Biomimetic coating for minimizing the invasiveness of brain interfaces, compatible with graphene bioelectronics

[a]Institut Néel, CNRS & Université Grenoble Alpes, 38042 Grenoble, France

[b]Université Grenoble Alpes, CERMAV, 38000 Grenoble, France

[c]Center for Neuroprosthetics and Brain Mind Institute, School of Life Sciences, Swiss Federal Institute of Technology (EPFL), Campus Biotech CH-1202 Geneva, Switzerland.

KEYWORDS. biomaterial, neuroprostheses, graphene, hyaluronan, bioelectronics, neural growth, brain implants.

ABSTRACT. Electronics or optical neural interfaces are broadly used for *in-situ* biosensing and electrophysiology. These neurotechnologies allow spike detection from single cells within large neural networks, which have enabled pivotal discoveries in brain sciences and neuroprosthetic treatment development. However, these rigid interfaces trigger foreign body responses within the soft and living neural tissues. These responses limit their resolution, efficiency and long-term reliability for chronic recordings, which are essential features for basic and applied research issues in brain science. Graphene bioelectronics offers many advantageous properties for interfacing biomatters. This material promotes neural regeneration and enables single spike detection with soft, transparent and flexible device arrays. However, neural interfaces fabricated with a single graphene monolayer are easily teared off during insertion in the brain and display degradation over time. To address these issues, we evaluated the affinity of neuronal tissues with natural biocoating derived from hyaluronic acid. We show that this biocoating promotes neurite regrowth and accelerates the healing process around neural probes. These biopolymers can be deposited over a wide range of substrates, opening various avenues for improving the bioacceptance of various neural interfaces, including graphene bioelectronics.

Introduction. In the early 90s, the emergence of the microelectronic industry enabled the development of microelectrode brain arrays that are able to detect spiking activity from multiple neurons over days and months. These neurotechnologies enabled pivotal discoveries in fundamental brain research and supported remarkable breakthroughs in neuroprosthetic medicine. However, the reliability of neural recordings and bioacceptance of the neural interfaces have restricted the spectrum of questions and applications that could be addressed with these neural probes. As of today, the immune response of neural tissues and poor adhesion of neurons onto the foreign electrode material still limit the spatial resolution and temporal stability of current neural interfaces.

The amplitude of extracellular signals is not only very low (few 10 to100 μV), but is also screened by the surrounding extracellular matrix. Consequently, detection of spiking activity from single cells requires inserting electrodes in close contact with the target neurons. While this activity is occasionally recorded from the surface of neural tissues, reliable recordings from multiple neurons are necessary linked to the chronic insertion of electrodes within the brain. Consequently, the biotolerance, mechanical compliance, topography, and chemical stability of implanted neural interfaces determine the characteristics and performance of neural probes.

Currently, penetrating neural interfaces suffer from a poor bioacceptance, which leads to tissue responses and device failures that renders the coupling with the surrounding cells ineffective. When inserting neural probes, the native mesh of neural cells is disrupted; the subsequent reorganization of the neural tissues involves a proliferation of glial cells, and to a limited extent, the regrowth of the disrupted axons or dendrites. This process leads to the formation of a thick layer of microglia and reactive astrocytes that encapsulates the implanted devices and thus prevents an intimate contact with the targeted neural cells.[1,2] In addition, the micro-movement of

the rigid implant triggers an inflammatory response that contributes to increasing the distance between cells and sensors. The growing layer of glial cells corals the signal coming from neurons, which reduce the signal-to-noise ratio over time.[3] Finally, the presence of reactive oxygen species and free imbalanced charge can damage the implanted electronics, both the devices and the passive layer, which lower the sensitivity, efficiency and time reliability of devices.[4]

Over the past decade, graphene have attracted numerous interests to alleviate some of the issues associated with chronic penetrating neuroelectronics. Its neural affinity,[5-7] chemical inertness, bendability[8] (>100GPa tensile strength), anti-corrosive and anti-oxidative properties[9,10] combined with low cost production of high quality graphene monolayer by CVD growth make graphene an ideal candidate to improve the biotolerance of electrodes.[11,12] The low quantity of inserted electrode material - one single layer of low reactive (sp2) carbon atoms – is an advantage to reduce the toxicity of neural probes. Moreover, the use of single graphene monolayer CVD grown provides an accurate monitoring of its structural integrity *in-situ* by simple impedance measurement. However, frictions with cells and tissues that occur both during the insertion and once implanted can scratch or tear off the thin graphene monolayers exposed at the surface of electrodes, leading to devices and sensing failure. Moreover, preliminary studies have reported possible biodegradation of graphene in vivo. [13-15]

To overcome these limitations, one promising approach is to functionalize the neural probes with biopolymers. This natural biocoating combines many advantages. First, both the thickness and biodegradation of biopolymers can be controlled in order to maintain a close and tiny contact with cells. Second, they can protect the sensing sites during insertion. Third, they may improve the match between the mechanical properties of the electrode interface and the soft tissue, which

has been linked with improved biocompatibility and bioacceptance.[16] Fourth, biopolymers create porosities that may provide biomimetic niches. Fifth, the biocaoting could offer new functionalities such as drug delivery to promote cell regeneration or improved adhesion.

While different biomacromolecules (polysaccharides, peptides, proteins) are often used for modification of graphene oxide, only few biocoating of pristine graphene have been reported yet. For instance, a polypeptide (poly-L-lysine) coating may significantly enhance the biocompatibility of chemical vapor deposition (CVD) grown graphene for interfacing neurons.[7] In recent years, Hyaluronic Acid *HA* has been widely used as a biomaterial for different clinical applications.[17,18] This anionic polysaccharide is a major component of the extracellular matrix of connective tissues.

The interactions of HA with cellular HA-binding proteins are important for cell adhesion, proliferation, wound healing, and the HA binding sites might provide the possibility for selective cell adhesion.[17] Moreover, when used as basal layer for further hydrogels functionalization, it could soften the interface and improve the compliance with the cells to promote neurite outgrowth,[19.] Moreover, HA may support delivery of growth factor for nerve regeneration.[20] Until now, only few examples of HA-coated electrodes have been tested in vivo[21,22] or in vitro (Pt, iridium microwire and silicon microelectrodes)[23,24]. The challenge here lies in the maintenance of electrode performance after the coating process. Also, because of its negative charge, hyaluronic acid alone does not promote neural cells outgrowth in culture, but when combined with positive poly-L-Lysine polymer it becomes an efficient coating for tissue repair.

Here, we show the positive impact of hyaluronan biofilms on the adhesion and outgrowth of primary hippocampal neurons in culture and the possibility to integrate it onto graphene

electronics. Prior to combining these versatile tools *in-vivo*, we tested these biopolymers onto commercial intracortical probes. Monitoring of single unit stability and neural cell responses following one month of implantation into the motor cortex of rats suggested that such bio-coatings may improve sensor efficiency and time reliability, and may reduce the gliosis around the implanted intracortical site.

Materials and methods

Biopolymer coating. For the HA/PLL multilayers deposition, the samples are exposed to hyaluronan solution (M_w=200kg/mol MEDIPOL Distribution, dissolved at 2mg/ml in 0.15M NaCl solution adjusted at pH 6.5) for 10 mins, rinsed in three successive baths in 0.01M NaCl solution during 5mins, and exposed to poly-L-lysine (2 mg/mL, Sigma-Aldrich), and then rinsed in 0.01M NaCL solution (pH 6.5). The procedure was repeated several times to obtain the desired number of bilayers (from n = 1 to 5). The alkylamino hydrazide derivatives of hyaluronic acid was synthesized from the *HA* solution (M_w=200kg/mol MEDIPOL Distribution) as previously described,[26] to enhance the adhesion of the hyaluronic acid on the hydrophobic graphene sample. On the hyaluronic acid backbone were grafted alkyl chain, with a substitution degree - number of substituent per repeating disaccharide unit of HA - DS = 0.1 and 0.2. For simplicity, the term alkylated is used for the alkylamino hydrazide derivatives of hyaluronic acid. The water used in all experiments was purified by a Millipore Milli-Q Plus purification systems, with a resistivity of 18.2 MΩ/cm. Samples are kept in stable pH solution (NaCl 0.01M) until their use to preserve the polymers integrity. Shortly before cells seeding, the buffer solution is rinsed and replaced by the attachment culture medium and primary hippocampal neurons (extracted from mousse embryo E16, see methods) are introduced in the solution with a seeding density of 150kc/ml.

Pure neuron culture and immunofluorescent staining. Neurons were extracted from hippocampus of mouse embryos (E16.5 pregnant mice from Envigo, killed by cervical elongation), dissociated and seeded with a density of 150 000 cells/cm^2 in attachment medium (MEM supplemented with 10% foetal bovin serum, 1% glutamine and 0.05% peniciline/streptomycine, Gibco). Neurons were then incubated at 37°C and 5% CO_2, and the attachment medium was replaced few hours later by glial conditioned culture medium, supplemented with AraC (1 mM) to suppress the glial proliferation. The glial conditioned medium is previously obtained by culturing glial cells from the cortex in attachment medium until confluency. The cells were then cultivated with serum free Neurobasal medium (Invitrogen) and the gial conditioned medium was collected after 48 h for subsequent use on neuron cultures.

For the immunofluorescent staining, neurons were fixed in 4% paraformaldehyde (10 min), permeabilized in PBS-0.25% Triton-X100, blocked in PBS-2% bovine serum albumin and finally immunostained with the anti-Synapsin (1:500, Millipore), anti-Tau (1:300, Millipore) and anti-YL1/2 (1:1000, BioRad) primary antibodies, and DAPI (1:1000, Sigma-eAldrich) for labeling the synaptic vesicles, the axon, the cytoskeleton and the nucleus respectively. Immunofluorescence images were collected using automatic Zeiss AxioImager M2 microscope, and the image processing was performed with ImageJ.[27]

Statistic. For cell density counting, soma are detected with particle analysis Image J plugin after picture conversion in 8Bits and threshold definition to extracted the background noise. Soma size has first been measured manually on a dozen of neurons per picture in order to define the average soma area to detect. For groups of cells, each soma cannot be discriminated, thus the number is estimated from the total area and soma size ratio and verified with manual counting. The covering rates for each stained surfaces (total neurite, axon, synapse surfaces) have been

extracted with the threshold tool in Image-J, preserving a constant brightness level for each fluorescent antibodies. Defocus - inducing less brightness and larger covering surfaces – is taking into account by keeping same threshold level of brightness between all pictures.

***In-vivo* assay.** Six Adult female Lewis rats (200-225 grams, N.23, Charles River, UK) were housed individually on 12-h light/dark cycle with access to food and water *ad libitum*. Before surgery, animals were first habituated to human presence and manipulation during 2 weeks. Stereotaxic fixation was performed after administration of 0.1ml of Dorbene anaesthesia and surgeries were performed under inhalant anaesthesia of 2% diluted isofluorane in 2 L/min oxygen. Briefly, 32– channel microelectrode arrays (n=3 active, n=3 control; Tucker–Davis–Technologies, USA) were inserted into layer V of the leg region of the right motor cortex, which we previously identified anatomically and electrophysiologically.[28] Signal amplification and recording were made with the Tucker Davis Technologies PZ2 preamp and RZ2 amplifier at the sampling frequency of 25 kHz. Spike sorting is processed in real-time by using TdT© OpenEx© commercial software and spikes of interest were stored when spike occurrence was matching with the walking status. We labeled the corresponding sensors among the 32 sensing sites of each implant. The experience was repeated once a week by in-cage free-movement recordings for all sensors and compared to previous results.

Histology. At the end of the experimental procedures, rats were perfused with Ringer's solution containing 100 000 IU/L heparin and 0.25% NaNO2 followed by 4% phosphate buffered paraformaldehyde, pH 7.4 containing 5% sucrose. The brains were dissected, post-fixed overnight, and transferred to 30% phosphate buffered sucrose for cryoprotection. After 4 days, the tissue was embedded and the brains sectioned in a cryostat (Leica, Germany) at a 40µm thickness.

Astrocytic and microglial reactivity was revealed by performing immunohistological staining against glial fibrillary acidic protein (GFAP) and ionized calcium binding adapter molecule 1 (Iba1), respectively. Briefly, the brain sections were incubated overnight with the anti-Iba1 (1:1000, Abcam) or anti-GFAP (1:1000, Dako) primary antibodies. Immunoreactions were visualized with appropriate secondary antibodies labeled with Alexa fluor® 488 or 555 (Life Technologies). Fluorescence counterstaining of Nissl substance was done using neurotrace 640/660 solution (1:50, Invitrogen). The brain slices were then observed with a laser confocal fluorescence microscope (Leica SPE, Germany) to estimate the glial cells population and density around the implanted probes. Immunostaining density was measured offline using representative confocal images of motor cortex sections. Images were acquired using standard imaging settings that were kept constant across rats. Images were analyzed using custom-written Matlab scripts.

Graphene substrates. Graphene monolayers have been grown by chemical vapor deposition on cooper foils (25 m m thick, 99.8% purity, Alfa-Aesar) according to reported protocol,[25] using pulses of CH_4 (2sccm 10s, then 60s off) flow in diluted H_2 atmosphere (1000 sccm, 25 mbar pressure) to prevent the development of multilayer patches. Prior the growth, the Cu foil has been cleaned in acetone and annealed in diluted H_2 atmosphere (10% in Ar) at 1000°C for 2h. Then, 4x4 mm graphene pieces are transferred on 12mm wide glass coverslip (Marienfeld) by polymer assisted wet transfer technique. The Cu foil, covered by PMMA resist on the graphene side, is wet etched in ammonium persulfate solution (0.1 g/ml, 2h). Once the Cu-etching is complete, the floating graphene-PMMA bilayer is rinsed with several washings in DI water to removed all traces of the toxic Cu-etchant solution, and fished with a cleaned and hydrophilic substrate (glass coverslips for the culture, or sapphire for device fabrication). The substrate coated with graphene-PMMA is dried at room temperature and PMMA is removed in an acetone

bath (overnight, room temperature). The transferred graphene sheets are then characterized using atomic force microscope and Raman microspectroscopy.

Field effect transistor array. As previously reported[29] the graphene sheet is etched to define 20 × 10 μm² wide and long transistor channels, by using photoresist mask and etching of the unprotected graphene parts with oxygen plasma. Then, this first photoresist mask is removed, and a second photoresist mask defines the negative pattern of the contact lead. A metallic thin film *Ti/Au* is then evaporated in vacuum, and the resist is removed in acetone bath. Finally, a biocompatible photo-sensitive polymer is used to insulate the contact leads from the top liquid and expose the graphene transistors channel only.

Results and Discussion

Neuritogenesis on hyaluronan polymers. Isolated hippocampal neurons have been cultured on the functionalized samples and compared to glass coverslip coated with poly-l-lysine *PLL* (control samples), to assess the bioacceptance of our hyaluronan biofilms. Because primary hippocampal neurons are highly sensitive to their microenvironment (topography, chemistry, surface charges, rigidity of the substrate and surrounding medium) in term of adhesion and neuritogenesis, they are suitable candidate to evaluate the affinity of an engineered interface.

HA is negatively charged, which thus prevents the adhesion and further growth of neurons because of the repulsive electrostatic interaction with the negatively charged cell membrane (figure S1, 20 samples tested). Therefore, we have combined *HA* monolayer with a positively charged polymer such as poly-L-lysine *PLL* which is currently used for neurons culture. In particular, we have deposited 5 bilayers of *(HA/PLL)* on conventional glass coverslip and compare those samples with the control *PLL* coated glass coverslips. As expected, while neurons

could not attach on the *HA* monolayers, the *HA_5/PLL_5* multilayers allow adhesion and neurites regrowth (figure 1a). The number of soma and length of neurites being almost twice higher and longer respectively than on single *PLL* monolayer (control samples) at DIV5 (figure 1b). Axonal differentiation and synaptogenesis are also enhanced on the multilayers in term of axon length and number of synapses. The higher adhesion and spreading rates observed on the multilayers certainly accelerate the maturation process.

The discrepancies with the *HA* coated samples cannot be explained by the presence of PLL only, as the adhesion and neurites outgrowth is higher on multilayer than on the *PLL* coated control glasses. The higher thickness and the specific topography of the multilayer could be additional features supporting the neural development. In particular, the presence biomimetic niches specific to *HA* topography have been shown to promote neurons adhesion and maturation.[30]Moreover, the rigidity sensed by neurons could be lowered on the thick multilayers and significantly impacts the neuritogenesis in comparison with the conventional PLL coated glass, the mechanical compliance between cells and substrate being enhanced on the 50 nm thick multilayers (Young's modulus ranging from kPa for HA/PLL multilayer to GPa for glass coverslips). The rigidity of the interface is indeed a key feature for the adhesion and spreading of numerous cells.[31] Also regarding our cultured hippocampal neurons, we have observed that neurites outgrowth is indeed significantly enhanced on soft (100kPa-MPa) PDMS substrate, in comparison glass coverslips (figure S1).

We have compared the impact of the surface charge by varying the biofilms top layer (last deposited), being either *HA* or *PLL*. And as expected, the (*HA_5/PLL_5*) multilayers (PLL on top) promote even further the neural adhesion outgrowth, the neurons and synapses density being higher than on the (HA_5/PLL_4) multilayers (figure 1a). These results show that surface charges

still impact the adhesion and spreading rates of cultured neurons, together with the mechanical compliance with cells and surface topography.

To investigate further the impact of the surface polarity on neurons adhesion and growth, we have engineered the repulsive and negatively charged *HA* monolayer, by adding alkyl chains (positively charged) on the polymer backbone (detailed in methods). We have then followed the development of neurons cultured on the alkylated *HA* (*α-HA*) monolayer deposited on glass coverslips. Surprisingly, after one day of culture, efficient adhesion and neurite spreading were observed on the *α-HA* monolayers, while neurons could not attach on the native *HA* coated glasses (figure S1). These results confirm the significant impact of non-covalent and non-specific electrostatic interactions such as the surface charge on the first stages of the neural development.

Brain neural cells responses. Although *in-vitro* assay remains mandatory to assess the bioacceptance and efficiency of biomaterials, cells could behave differently when cultured on flat samples than *in-vivo* in their 3D native scaffold. To investigate the response of brain cells, we have deposited the HA_5/PLL_5 biofilm on commercial neural probe, and follow the impact of the coating on the bioacceptance of the electrodes, in term of cell response (neurons regrowth versus glial cells proliferation) and of device performance (single spike detection efficiency and reliability).

Intra-cortical implants are one type of the neural probe which faces the most rejection and poor reliability, because it penetrates and disrupts several layers of the brain architecture. Despite tissues damages caused by the implantation surgery, they are still the only tools able to monitor neurons activity with single spike resolution in freely moving animals, and are thus widely used for neuro-rehabilitation research. For that purpose, we have investigated the impact of our

biofilms on the bioacceptance of such neural probe inserted in the motor cortex of rats. We have compared 3 functionalized probes and 3 control (uncoated) probes, each probe being constituted of 32 independent microelectrodes (tungsten wires, Utah Array, from Tucker Davis, figure 2a). The targeted axonal projections of motor neurons are located in the IV-V cortical layers, involved in the hindlimb locomotion command.[32,33] Recordings were performed once a week with a freely moving recording of the 6 rats, during 7 weeks after the implantation surgery. After 1 month, the recordings were performed during walking controlled motion and compared with the muscle kinetic and locomotion behaviours. The detected neural spikes are extracted from the time traces voltage of the 32 electrodes which have been acquired during mouse walks on a treadmill and further analyzed in term of shape, amplitude and frequency to track motor neurons spiking activity (figure 2b). The electrodes which successfully detect spiking events from motoneurons were followed along the 7 weeks.

During the 7 weeks, clear signals (with high signal to noise ratio, S/N>3) were extracted with all the 3 functionalized probes, while only 1 (uncoated) control probe showed similar high quality signals. Spikes were indeed regulars and synchronized with trunk and legs movements, suggesting efficient interfacing of motor neurons (figure 2c).

Disruption of the blood vessels during the implantation surgery could be a source of variability, because of the large amount of blood macrophages and endothelial cells carried inside by the implant could increase the proliferation of astrocytes (gliosis) leading to detection failure (figure S2 and S3). However, functionalized electrodes were still able to sense and discriminate single units (motor neurons spike) during highest bleeding level (5/5), while no signal was recorded with the bare (uncoated) probes at a lower (4/5) bleeding level, which further demonstrates the positive impact of the multilayers.

The density of astrocytes and microglial were assessed post-mortem using histochemistry (figure 2e and figure S3). In agreement with an improved detection efficiency of neural spikes, the number of microglial (Iba1) was reduced when probes were functionalized. A lower density of astrocytes (GFAP) was also found (figure 2f). These results suggest that the coating reduced foreign body response, which is consistent with the improved quality of recordings.

These results provide evidence suggesting that hyaluronan film does not alter neural activity and enhances the detection efficiency, mediated by a better coupling to the healthy cells. While further statistical tests are required, such biopolymers appear promising for enhancing the bioacceptance of intra-cortical probes.

Compatible with graphene bioelectronics. Graphene is emerging as the future bionic electrodes material for interfacing biological objects, in particular neural networks. It provides a unique combination of exceptional properties suitable for bio and neuroelectronics, such as high conductivity, interfacial capacitance, chemical inertness, optical transparency, and flexibility, associated with anti-corrosive and anti-oxidative properties. We have compared the neural affinity of several neural interfaces such as graphene, PDMS, diamond, polyimide, parylène and conventional glass coverslips (figure S4) and the improvement gained by hyaluronan biofilms and graphene are clearly significant for neurons regeneration.[7] For that purpose, we have investigated the adhesion of hyaluronan based biofilms onto graphene monolayers and assessed its impact on the electronics properties of graphene field effect transistors, which emerge as the next candidate for nanoscale addressing with multimodal and long lasting neural probes.[34]

Indeed, the combinaison of hyaluronan and graphene neuroelectronics can open new perspective for improving the chronic bioacceptance of neural interface. In addition to many suitable

properties of graphene for interfacing living matters, HA biofilms could favor healing and regeneration processes, protect the single graphene monolayer during insertion and serve as an active support for delivering drug or growth factor. In addition, the degradation of the HA biofilms with natural enzyme may support the restoration of a direct contact with the cells and the underneath materials, which favor improved sensing.

Because graphene functionalization can disturb both its electronics properties and its crystalline quality, we have comprehensively assessed the adhesion of the hyaluronan monolayer on high quality CVD grown graphene monolayers by Raman spectroscopy and atomic force micrographies. Figure 3b shows a representative Raman spectrum (λ_e=488nm, with a Jobin Yvon T64000 Raman spectroscope) obtained on the *HA*-coated graphene samples. The presence of *HA* is confirmed by the appearance of low frequency resonant modes (899- 950 cm^{-1}, 1090 cm^{-1}, 1180 cm^{-1}, 1410-1460 cm^{-1}) characteristic of *HA* polymer.[35,36] The contributions of carboxyl and methyl groups (CH and CH_3, COO^- expected at 1330 cm^{-1} and 1370 cm^{-1} respectively) should be surimposed with the defects-related D-band peak (1350 cm^{-1}) of graphene. However, the amplitude of the D-band peak (1352 cm^{-1}) remains low $I_{D/G}$<0.06 even after HA functionalization, revealing low quantity of lattice defects.[37] These results show that the hyaluronan monolayer and the coating process do not alter significantly the crystalline quality of the graphene monolayer.

The atomic force micrographs (figure 3c-e) performed before and after functionalization reveal the integrity and quality of the graphene monolayer, previously transferred on glass substrates. The *HA* monolayer deposited on graphene appears rather granular and agglomerate at the graphene wrinkles, certainly because graphene is highly hydrophobic. Indeed, the overall homogeneity of the coating is significantly enhanced by adding hydrophilic chains on HA

polymers (figure 3a and 3e). Contact angle measurements show the increasing hydrophilicity of the functionalized graphene monolayer when increasing the density of the (positively charged) alkyl chains grafted on the *HA* backbone (figure 4).

We have then assessed the large scale homogeneity of *HA/PLL* multilayers deposited onto graphene substrate. Taking advantage of the quenching properties of graphene,[38] we have stained the top PLL layer with FITC, the last layer deposited during the multilayer assembly. Figure 4a shows clearly the frontier between the quenching graphene and the glass substrate which exhibits higher fluorescence intensity. The quenching effect - induced by the underneath graphene monolayer - decreases with the number of deposited *HA/PLL* bilayer. As shown in figure 5a et 5b, the ratio of fluorescence intensity is reduced by 48% from 1 to 5 bilayers, being about 2.4 and 1.24 respectively (thickness of 1 layer d_{1L}~ 5 nm), confirming that the distance to graphene is increasing during the multilayer assembly. Interestingly, periodic oscillations of the fluorescent intensity reveal biofilm ripples at the graphene/glass interface (zoomed view figure 5b), suggesting the appearance of mechanical strains in the multilayer assembly above graphene.[39]

We have measured the impact of the biocoating on the transport properties of graphene field effect transistor *GFET*. Several GFETs have been fabricated on sapphire substrate (figure 6b) and their transconductance $g = \partial I_{DS}/\partial V_G$ - normalized by the drain voltage V_{DS} - were measured before and after functionalization giving the impact on the GFET sensitivity S :

$$S = \frac{\Delta G}{G} = \frac{\partial I_{DS}/\partial V_G}{V_{DS}} \times \frac{1}{G}$$

with G the conductance of the graphene transistor channel, I_{DS} the drain-source current and V_G the liquid gate voltage applied with a quasi-reference Pt-electrode (figure 6a). The dependence with V_G of the 10×20 µm² GFET channel current shows a symmetric ambipolar field effect behavior with a charge neutrality point at $V_D \sim 0.4$ - 0.5 V (figure 6c). The sensitivity S reaches its maximal value at the inflections of the field effect curve where the slope is the highest.

While *PLL* does not affect the GFETs properties,[29] *HA* monolayer (red curve) reduces the transconductance and shifts the Dirac point toward more positive values, in agreement with the overall negative charge of *HA* polymers. However, the minimum of conductance remains however unaffected, confirming that *HA* does not damage the integrity of the graphene devices. The reduced transconductance could stem from reduced charge carrier mobility, but also because the hyaluronan film changes the interfacial capacitance C_{LG} previously defined by the double electrical layer capacitance only ($1/C'_{LG} \sim 1/C_{HA}+1/C_{EDL}$). The interfacial capacitance and in particular the double layer capacitance C_{EDL} at the graphene/liquid interface are not directly measurable, C_{EDL} being depends on the geometrical (Helmotz and diffusive) and quantum capacitances of graphene ($1/C_{EDL'} \sim 1/C_{Ge}+1/C_Q$) which is the smallest and function of the liquid gate.[40]

Thus we have extracted the interfacial capacitance and carriers mobility from the transfer curve I_{DS}-V_{LG}, according to previous methods for liquid gated GFET, describing the conductivity of graphene transistors in (top) liquid gated configuration as function of the fermi level and scattering induced by adsorbed impurities and defects: [41,42]

$$\sigma = C.\frac{L}{W} = g_0 \frac{6\sqrt{3}}{4\pi}\frac{a_0^2 \alpha}{n_i}|V_{LG} - V_D| ln^2(\sqrt{\alpha\pi|V_{LG} - V_D|}r)$$

with g_0 (0.039mS) the quantum of conductance, a_0 (1.42 Å) the C-C lattice bond length in graphene, n_i the density of impurity or defect, α (=n/V_{LG}) a model interfacial capacitance, and $r \sim a_0$ the short range potential induced by defects scattering.

By varying the density of defects n_i and the idealized capacitance α, we have fitted the conductivity of our GFETs as function of the liquid gate, before and after HA deposition (figures 6e and 6f). As expected, adding HA results in increasing slightly the defects density n_i, from 0.5 to 0.66 $\times 10^{12}$ cm^{-2}, while the total interfacial capacitance ($C_G=\alpha \times e$) is reduced from 0.56 to 0.53µF.cm^{-2}; the total interfacial capacitance including the serial contribution of the electrical double layer at the interface with the Pt reference electrode, the HA capacitance and the second electrical double layer capacitance at the interface with graphene. From those values, we can estimate the carriers mobility: $\mu_{h,e} = L \times g_m/(W \times V_{DS} \times C_G)$, with g_m the maximum transconductance for holes and electrons respectively extracted from the transfer curve $\partial I_{DS}/\partial V_G$ (V_G) at the maximum inflection point. On bare GFETs, holes and electrons mobility are asymmetric, being higher in the hole conduction regime μ_h=1881 cm²/V/s (and μ_e=1631 cm²/V/s), in agreement with previous values for GFETs[43] After HA deposition the hole and electron mobility are slightly reduced, being almost the same $\mu_{h,e}$ = 1283 – 1296 cm²/V/s for holes and electrons respectively.

These results provide first insights for the use of hyaluronan biofilms in neurotechnology. Further investigations should be done with customized HA polymers to lower its impact on the carriers mobility, and keep high sensitivity values such as obtained with its counterpart positively charged poly-L-lysine polymers. The controlled enzymatic degradation of the biocoating[44] should also be investigate as it provides an alternative way to restore progressively a direct

contact with cells at the sensing area and still improve the healing process and regrowth of neurons around the electrodes. In that way, hyaluronan films would still provide a protective biomimetic shell for inserting rigid and foreign neural probes through tissues, preventing graphene tear off or delamination during implantation surgery.[13]

Conclusion

We showed that HA biofilms improve the adhesion and outgrowth of cultured hippocampal neurons, appearing as a highly biocompatible and active substrate for nerve regeneration. Evidence suggested that using this coating to functionalize cortical implant reduces astrocytes and microglial proliferation around the probe. This reduced foreign body response was associated with improved single spike detection and time reliability. While further investigations are required to confirm the observed trends and to understand the mechanisms underlying the healing process, these results open promising perspectives for expanding the lifetime and reliability of brain implants. Hyaluronan acid is indeed the basement of further functionalization such as natural hydrogels that could provide new functionalities for delivering drug, stem cells or growth factors. The possibility to combine it with graphene bio/neuroelectronics provides exciting solutions to prevent possible delamination of graphene monolayers *in-vivo*, to improve healing process and the electrical coupling to neurons, and to provide new strategy for nerve regeneration. These biodegradable polymers will be helpful for improving the bioacceptance of a wide range of biomaterials used in neuro- and biotechnology.

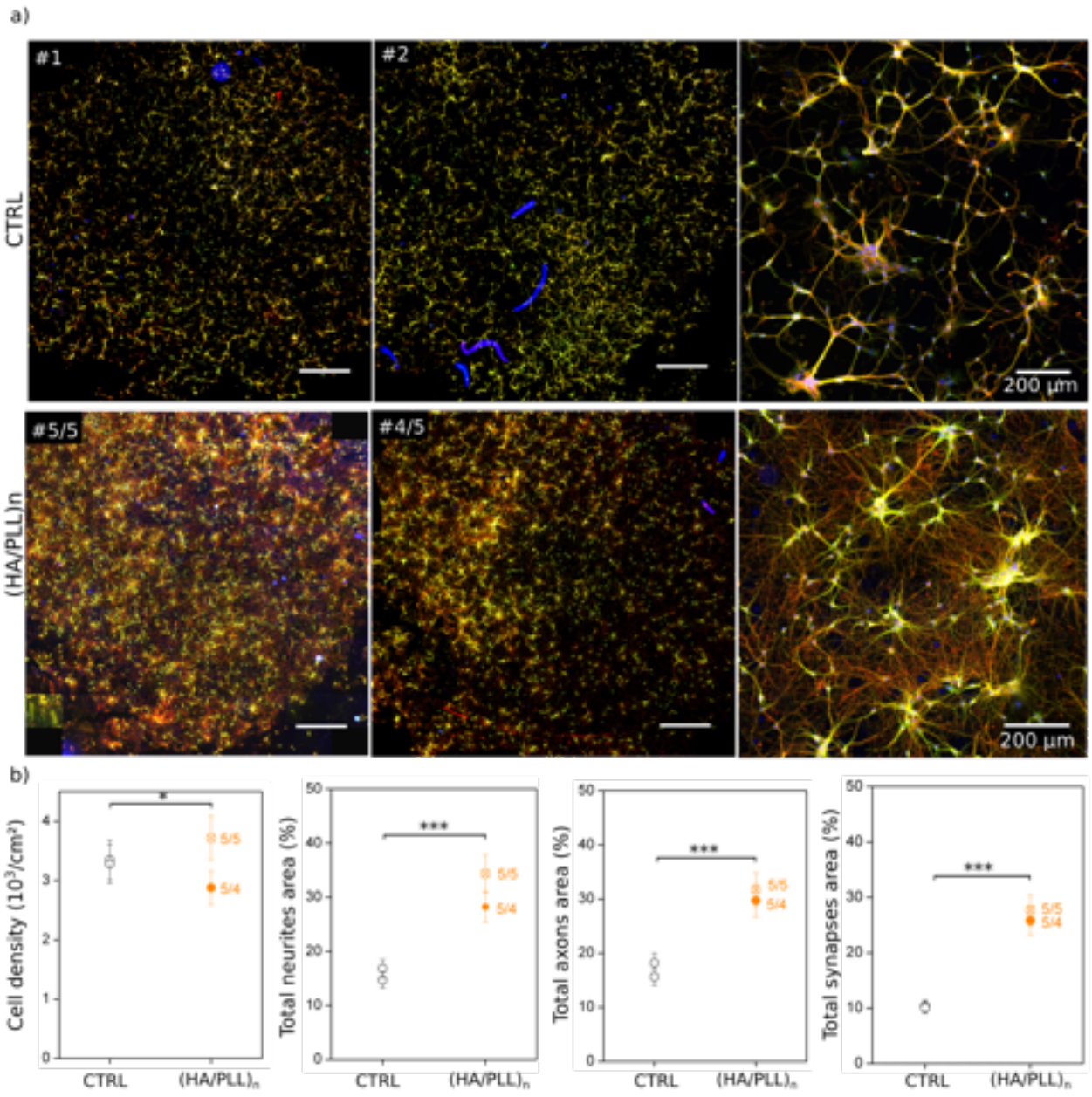

Figure 1.

Figure 1. Neuritogenesis on hyaluronan biofilms. (a) Immuno-fluorescent micrographs of primary hippocampal neurons cultured 5 days on glass coverslips coated with PLL (CTRL samples) and (HA/PLL) multilayers; the last layer being *PLL* (5/5) and *HA* (5/4) respectively. The soma, neurites, axons, and synapses are labeled in blue (DAPI), green (YL1/2-FITC), infrared (Tau-CY5) and red (Synapsin-TRITC). Scale bars 100µm. On the right, zoomed views of the *PLL* control samples and the *HA/PLL* multilayers respectively. (b) Statistic analysis comparing neuron density and total surface covered by neurites, axons and synapses on the several substrates (significant level *p<0.1, *** p<0.001).

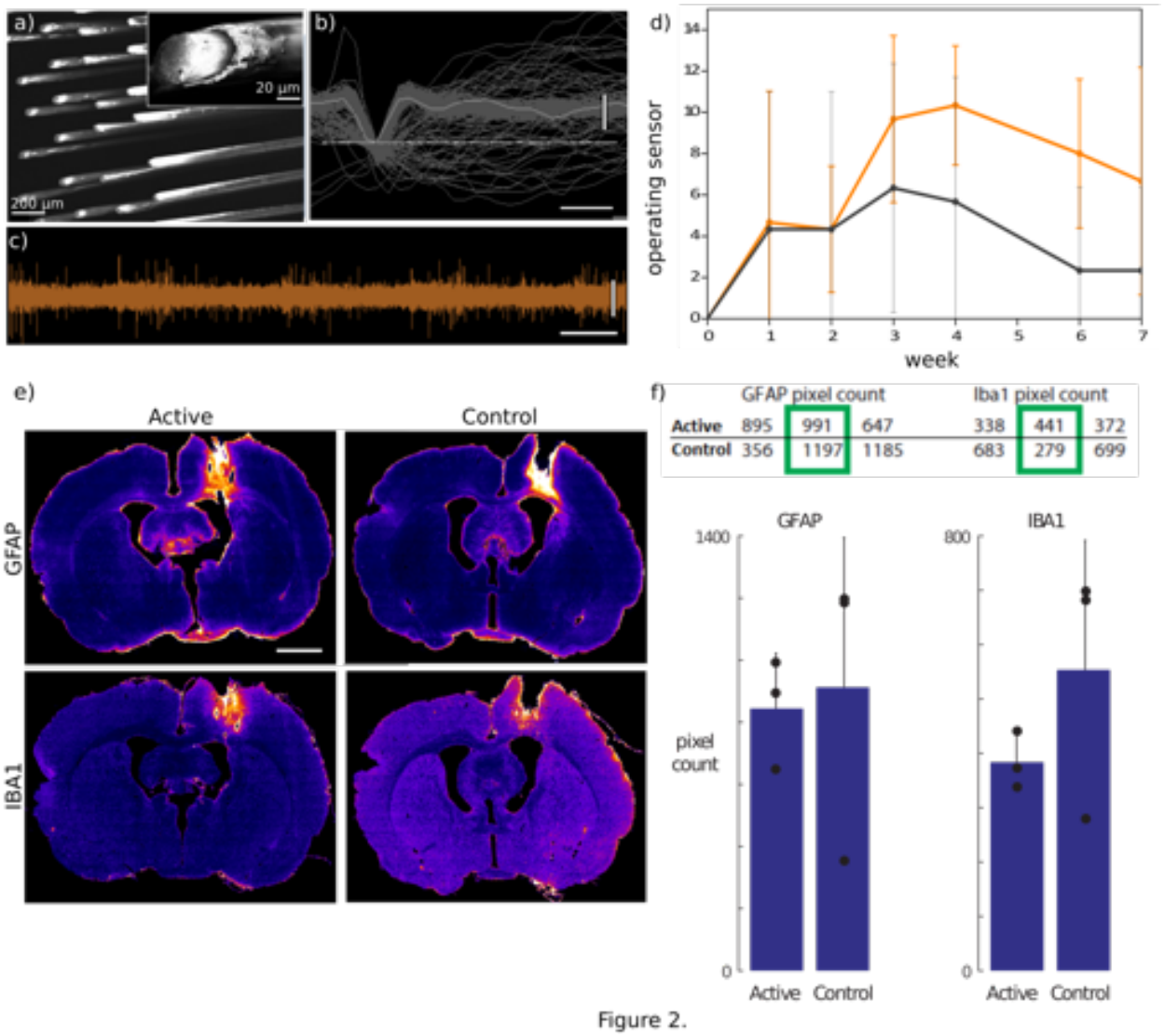

Figure 2.

Figure 2. Hyaluronan biofilms deposited on neural probes. 5 HA/PLL bilayers were deposited on commercial tungsten electrodes arrays (TDT array) implanted in motor cortex of rats and compared to control samples (same probes without coating). (a) Fluorescent micrographs of the coated electrodes. FITC (λ_{exc}=488-nm) molecules have been grafted on the top (last deposited) *PLL* layer. (b) Typical single unit spiking activity superimposed and extracted from the time trace of the extracellular voltage shown in (c), recorded 7 weeks after the implantation during locomotion. Scale bar 100µV and 1ms. (d) Percent of electrodes from which spiking activity could be detected in the control (black) and functionalized (orange) probes. (e) Post-mortem immuno-fluorescent micrographs of the tissues at 4 weeks after implantation surgery, showing astrocytes (GFAP) and microglias (IbA1) proliferation around the coated and bare electrodes (left and right respectively). Scale bar 2mm (f) The table compares the total surface

covered by astrocytes and microglias for all the 6 probes; the corresponding IF micrographs are shown in figure S3. The green squares underline the result obtained from (e).

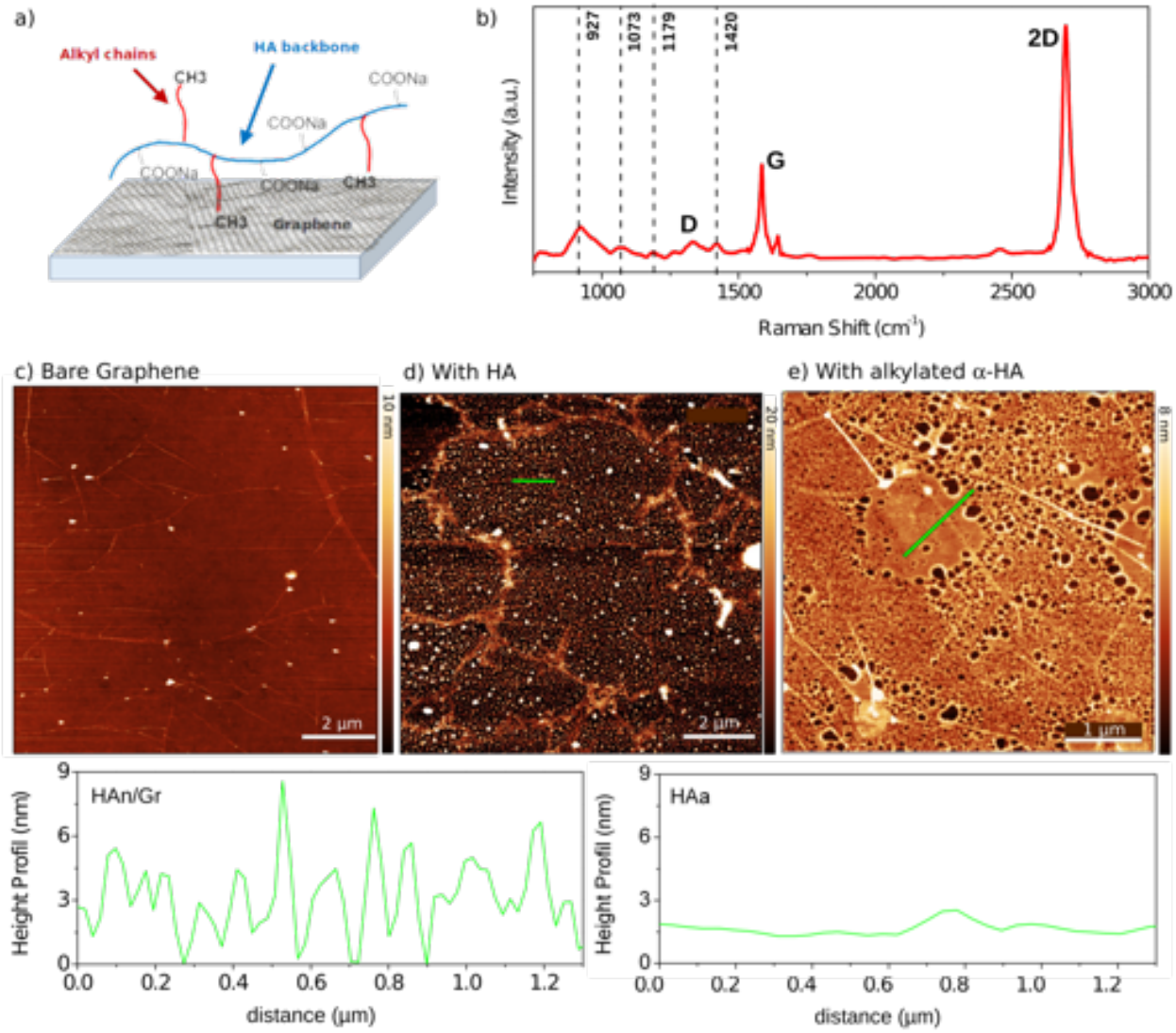

Figure 3.

Figure 3. Hyaluronan adhesion onto graphene. (a) Schematics of the biopolymer customization for a homogeneous adhesion on hydrophobic graphene monolayers. The *HA* backbone is functionalized with alkylated hydrophobic *(CH_3)*-chains promoting polymer attachment onto the hydrophobic substrate. (b) Typical Raman spectrum acquired on *HA*-coated graphene samples, showing several peaks of the hyaluronan and graphene monolayers. The mains resonance of *HA* are resolved, underlined with the dashed lines. The intensity ratio I_G/I_{2D}~0.2 between the 2D and G-bands peaks is characteristic of one graphene monolayer. Also, the low intensity of the D-band peak confirms the overall high crystalline quality of the graphene monolayers even after functionalization. (c-e) Atomic force micrographs of

typical bare graphene monolayer transferred on glass (c), then coated with *HA* (d) and alkylated *α-HA* (e) monolayers, with the corresponding z-profiles of the two coatings (left: *HA,* right: *α-HA*) measured along the green line in (d) and (e).

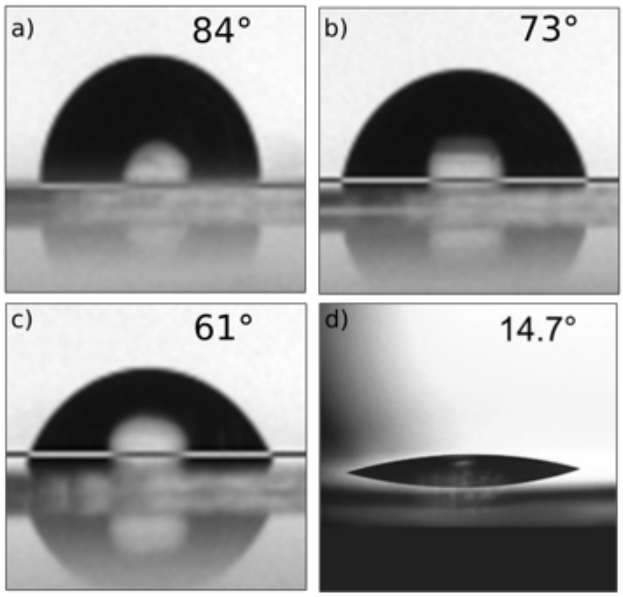

Figure 2.

Figure 4. Drop angle measurements on α–HA coated graphene samples as function of the alkyl chains density, compared to bare graphene previously transferred on glass coverslips. As expected, the contact angle decreases when increasing the degree of substitution with the alkyl chains from: (a) DS=0 (bare graphene), (b) DS = 0.1, (c) DS=0.2.(d) *PLL*-coated glass (control samples).

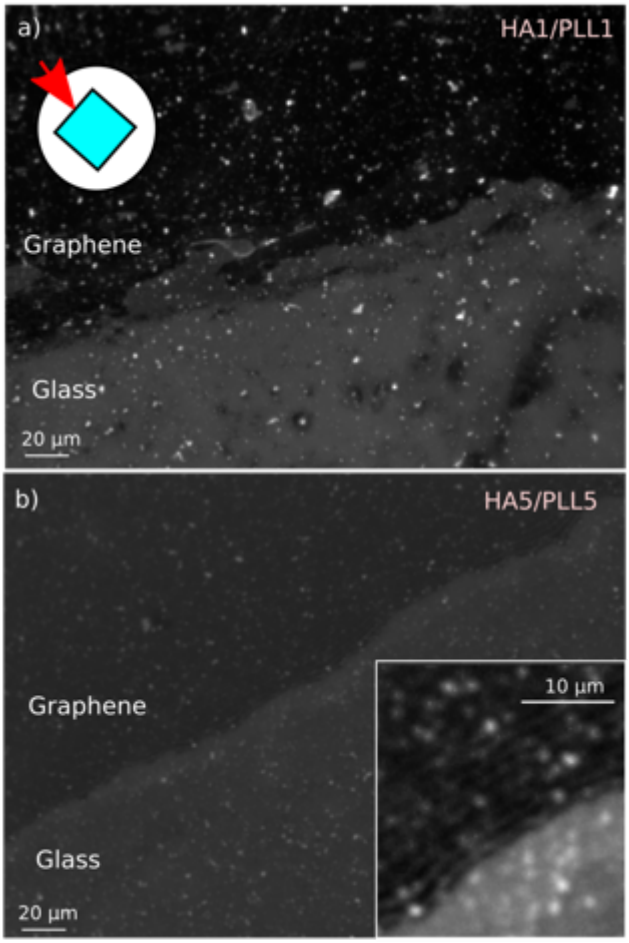

Figure 5.

Figure 5. Homogeneous multilayers deposition on monolayer graphene. Fluorescent optical micrographs of 1 (a) and 5 (b) *HA/PLL* bilayers deposited on a 4×4mm² piece of graphene previously transferred on glass coverslips (depicted in blue on the scheme). FITC (λ_{exc}=488-nm) molecules have been grafted on the top (last deposited) *PLL* layer. Exposure time is 1500ms (a), and 500ms (b). The quenching effect produced by the graphene monolayer (darker area) is clearly observed at the frontier with the glass substrate, and decreases when the distance to the FITC molecules is increasing, by depositing more layers. The ratio of fluorescent intensity above graphene and the bare glass I_{Gr}/I_{Gl} is reduced by 48%, ranging from 2.4 (a) to 1.24 (b) for 1 to 5 *HA/PLL* bilayers (thickness d_{1BL} ~ 5 nm). Inset: zoomed view of the frontier with graphene. A periodic interference pattern appears, revealing mechanical strains in the multilayers assembly above graphene.

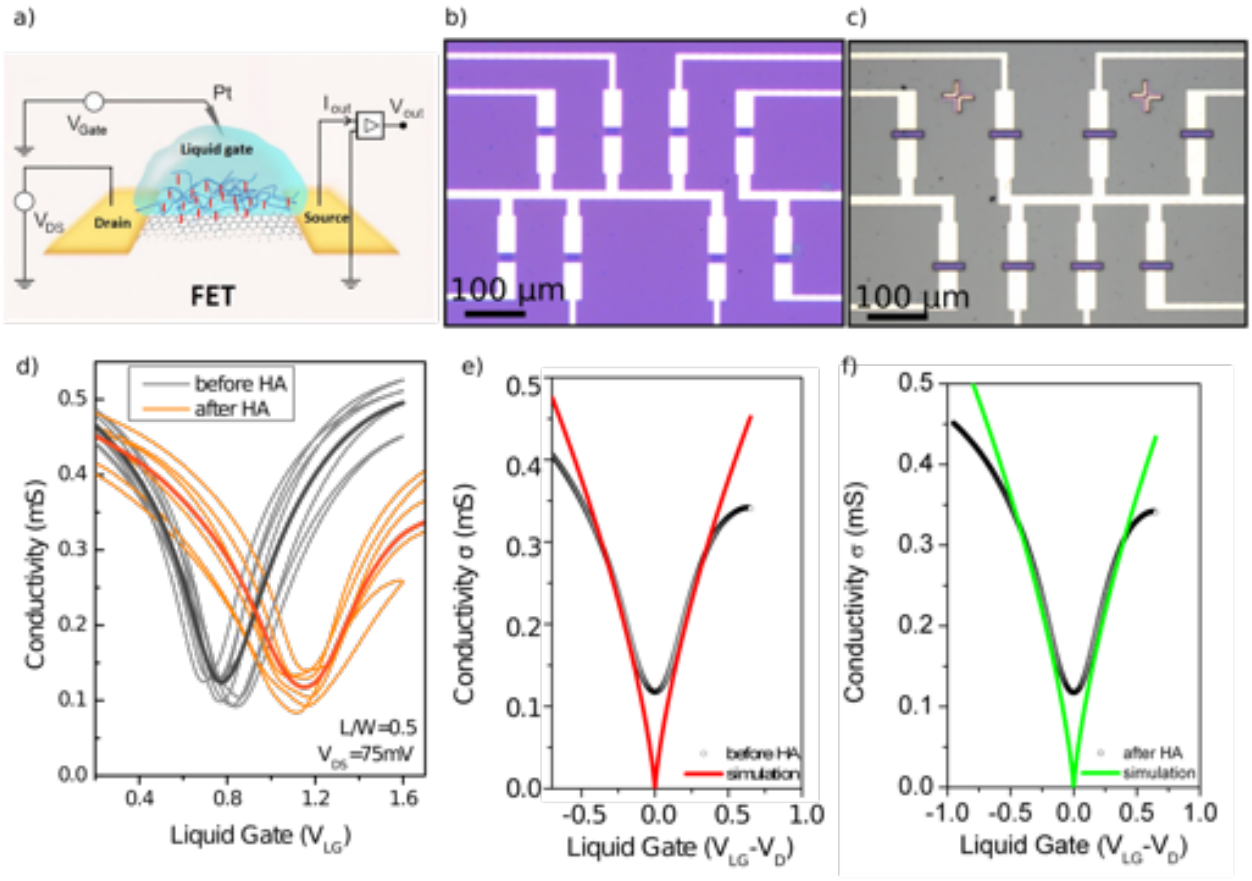

Figure 6.

Figure 6. Impact of hyaluronan on the electronics properties of GFETs. (a) Schematics of the graphene field effect transistors *GFETs*. The electrical equivalent circuit illustrates the coupling between the liquid gate and the graphene FET channel. Optical micrographs of the GFETs array before (b) and after (c) the passivation of the Ti/Au metallic leads. The graphene FET channels are 10×20µm long and wide. (d) The GFET conductance - before (gray) and after (red) *HA* deposition – is recorded as function of the liquid gate voltage V_{LG} applied with a quasi-reference Pt electrode. Each curve corresponds to one device. Thicker curve is the mean average value over all tested devices. The average curves are fitted to extract the charge carriers density and mobility, before (e) and after (f) functionalization (fit details are in main text).

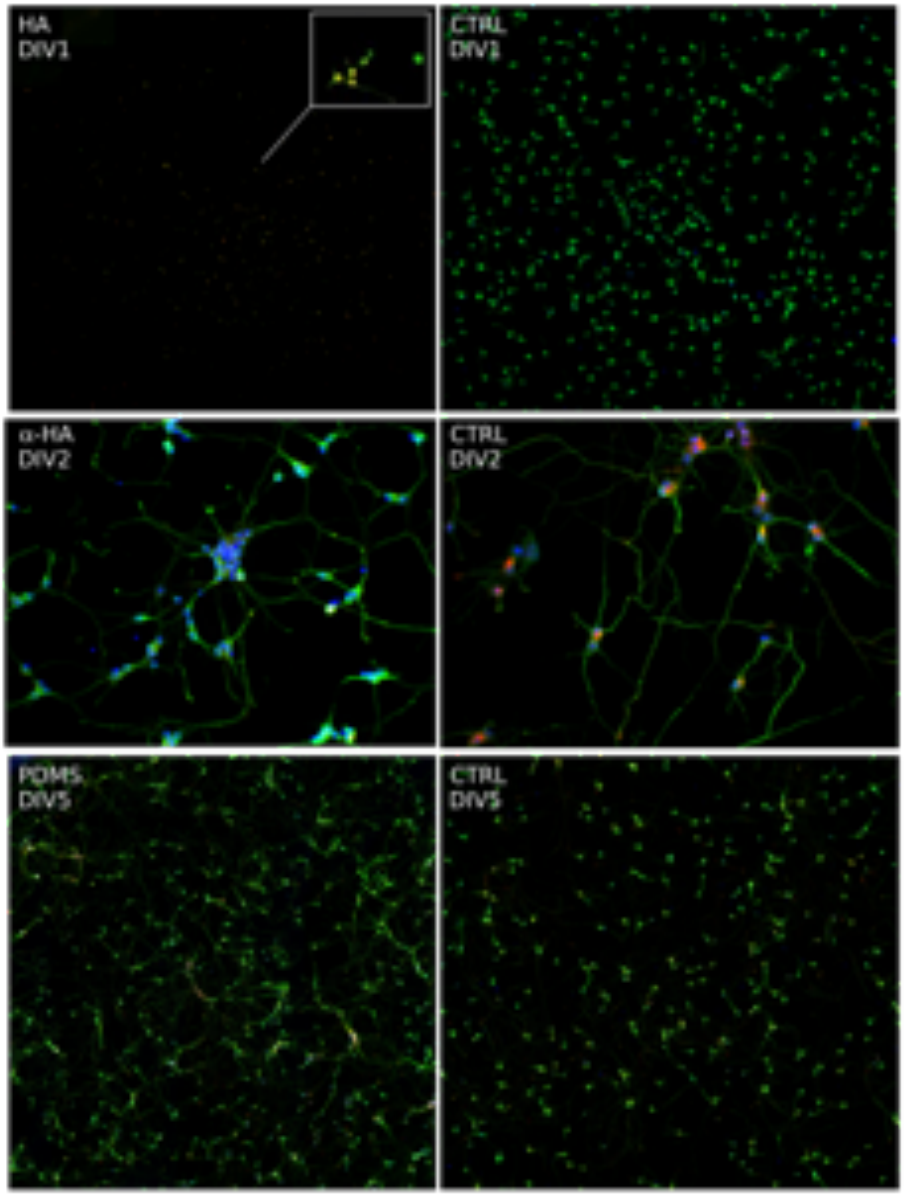

Figure S1

Figure S1. Neurons adhesion and growth on several polymers. Immuno-fluorescent micrographs of primary hippocampal neurons cultured on single monolayer of HA (a), α-HA (b) and on PLL coated PDMS (c), compared to control samples (PLL-coated glass). The soma, neurites and synapses are labeled in blue (DAPI), green (YL1/2-FITC), and red (Synapsin-TRITC) respectively.

	Functionnalized - HA/PLL 5 Bilayers coated TDT electrodes arrays		
	#478	#479	#480
Surgery	Brain Vessel size = 2/5 . Bleeding = 1/5	Brain Vessel size = 3/5 . Bleeding = 2/5	Brain Vessel size = 5/5 . Bleeding = 5/5
W+1	Weak signal	Good signals/best channels: 23,29, 24XL	Weak signal
W+2	Good signals	Good signals	Almost silent except ch16
W+3	Good signals/best channels: 11,14XL,27	Good signals/best channels: 20 , 31XL	Good signals
W+4	Walk OK kinetics on ch 13XL, 11, 6, 15	WALK OK kinetics on ch 15,20	WALK OK kinetics on ch 16
W+6	Good signals	Good signals/best channels: 15,24XL, 27XL	Good signals/best channels 1, 16
W+7	Good signals	Good signals/best channels: 14,15,24	Almost silent except ch16
	Control - out of the box TDT electrodes arrays		
	#481	#482	#483
Surgery	Brain Vessel size = 4/5 . Bleeding = 4/5	Brain Vessel size = 1/5 . Bleeding = 1/5	Brain Vessel size = 4/5 . Bleeding = 5/5
W+1	Weak signal	Good signals/best channels:6XL,8XL,31XL	Silent
W+2	Almost silent except ch 24, 13	Good signals	Silent
W+3	Ch 22XL	Good signals/best channel: 27 XL	Silent
W+4	Almost silent exept ch 24	WALK OK kinetics on ch 24	Silent
W+6	Silent	Good signals/best channel: 7,27,25,6,7	Silent
W+7	Silent	Good signals/best channel: 7,11,12,14,27	Silent

Figure S4.

Figure S2. Surgery and recordings sum up for the 2 group of rats, implanted with functionalized probe (#478, #479, #480) and control probe (#481, #482, #483). Color code shows signal global quality: green when several electrodes allow neuron recordings, yellow for only 1 working electrode and red when implant is silent. (32 electrodes per probe).

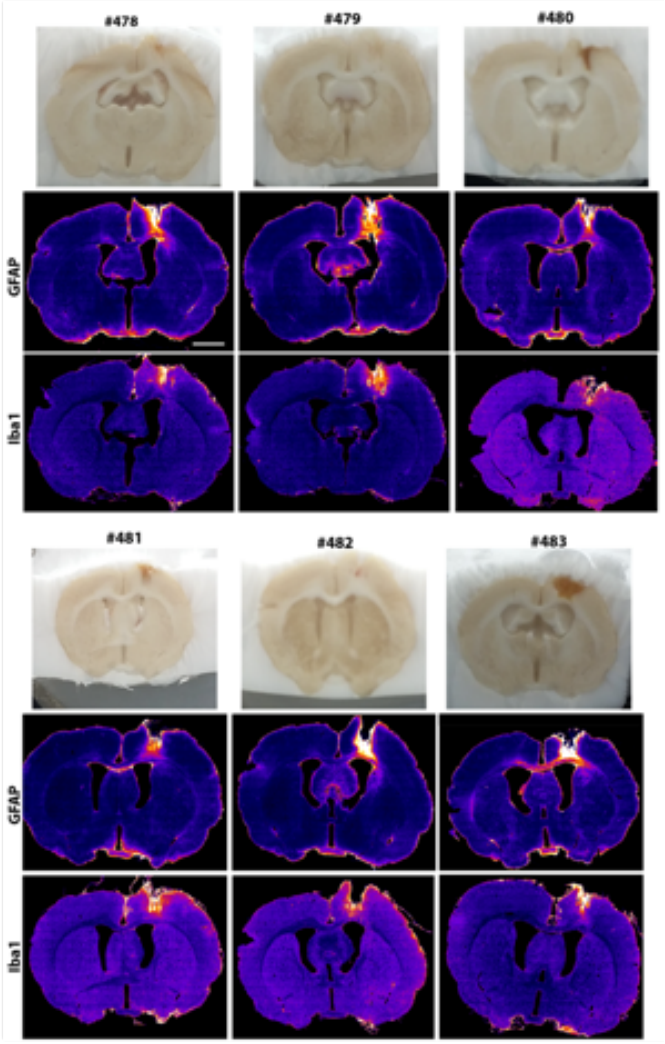

Figure S3.

Figure S3. In-vivo assement of hyaluronan biofilms deposited on the neural probes. 5 HA/PLL bilayers were deposited on commercial tungsten electrodes arrays (TDT array) implanted in motor cortex of rats (#478, #479, #480) and compared to control samples - same probes without coating- ((#481, #482, #483). Post-mortem optical and immuno-fluorescent micrographs of coronal slices, 4 weeks after the surgery and 48hfter implant removal, showing astrocytes (GFAP) and microglias (IbA1) around the coated and bare electrodes. Scale bar 2mm.

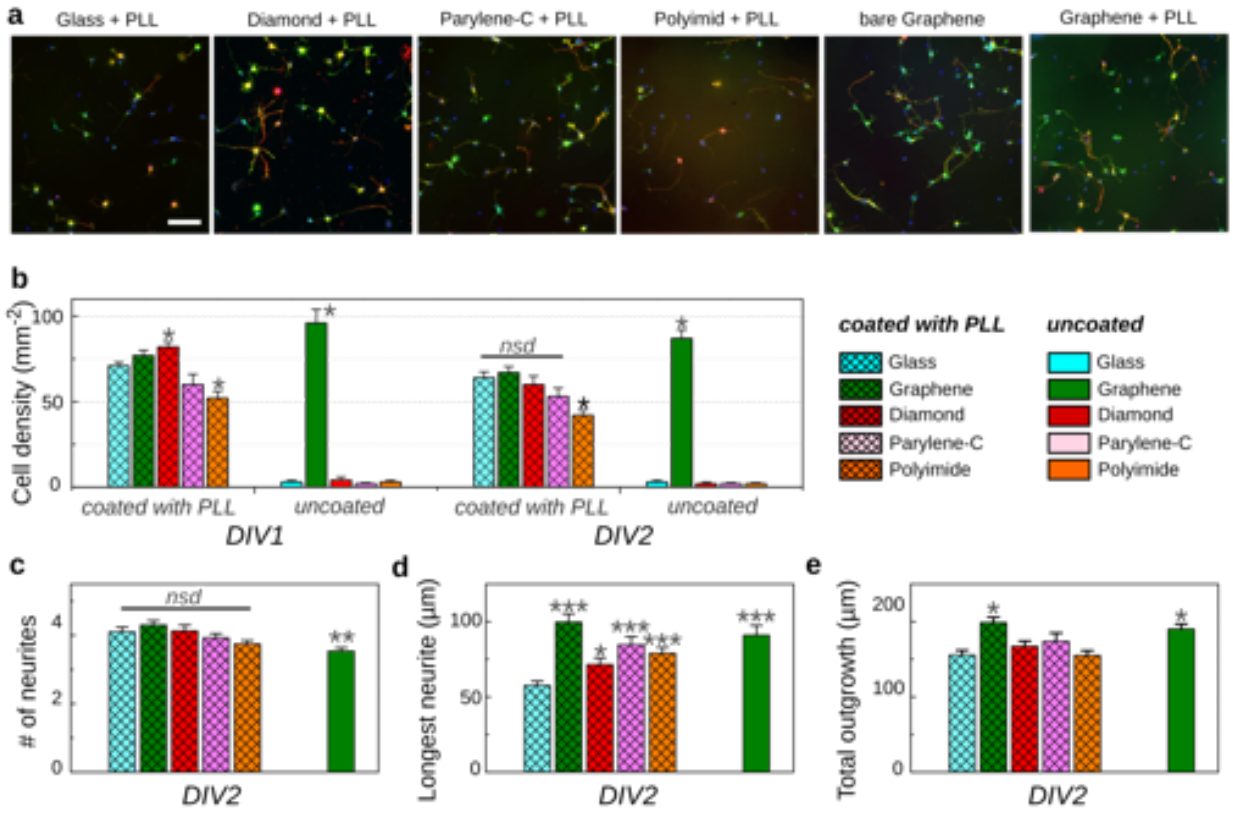

Figure S4. Neurons adhesion and growth on several materials commonly used for neural probes. (a) Representative immuno-fluorescent micrographs of 2 days old neurons growth on different substrates. In absence of PLL neurons only attach and grow on graphene. Dapi (blue) labels the soma, synapsin (green) the synaptic vesicles, and tau (red) the axon. Scale bar is 100 µm. (b) Neuron density at DIV1 and DIV2, (c) number of neurites, (d) length of the longest neurite and (e) the total outgrowth per neuron at DIV2. The results are obtained from one culture with two samples per batch and expressed as mean values ± s.e.m. (with at least 140 neuron per condition). The results were statistically compared to the control PLL coated glass coverslip using ANOVA followed by Bonferroni test with significance levels: $*p < 0.05$, $**$ $p< 0.005$ and $***$ $p < 0.001$, "nsd" means no significant difference.

ASSOCIATED CONTENT

Supporting Information. Supplementary figures S1-S4.

AUTHOR INFORMATION

Corresponding Author

*E-mail: cecile.delacour@neel.cnrs.fr

Author Contributions

The manuscript was written through contributions of all authors. All authors have given approval to the final version of the manuscript.

Notes

The authors declare no competing financial interest.

ACKNOWLEDGMENTS

The authors thank O.Bourgeois and the platform of biotechnology BioFab of Néel institut. The authors gratefully acknowledge financial support from the french Agence Nationale de la Recherche under the projects ANR-10-LABX-51-01 (Labex LANEF du Programme d'Investissements d'Avenir) the Lab Alliances on Nanosciences - Energies for the Future; and from la Région Rhône-Alpes (COOPERA project).

ABBREVIATIONS

HA. Hyaluronic Acid. PLL Poly-L-Lysine

REFERENCES

1. Polikov VS, Tresco PA, Reichert WM. (2005) Response of brain tissue to chronically implanted neural electrodes. Journal of neuroscience methods, 148 1-18

2. Barrese, J. C., Rao, N., Paroo, K., Triebwasser, C., Vargas-Irwin, C., Franquemont, L., and Donoghue, J. P. (2013). Failure mode analysis of silicon-based intracortical microelectrode arrays in non-human primates. Journal of neural engineering, 10(6), 066014

3. Lacour, S. P., Courtine, G., Guck, J. (2016). Materials and technologies for soft implantable neuroprostheses. Nature Reviews Materials, 1, 16063

4. Barrese, J. C., Aceros, J. and Donoghue, J. P. (2016) Scanning electron microscopy of chronically implanted intracortical microelectrode arrays in non-human primates. J. Neural Engineer. 13, 026003

5. Park, S. Y., Park, J., Sim, S. H., Sung, M. G., Kim, K. S., Hong, B. H., Hong, S. (2011). Enhanced differentiation of human neural stem cells into neurons on graphene. Advanced Materials, 23(36)

6. Li, N., Zhang, X., Song, Q., Su, R., Zhang, Q., Kong, T., Liu, L., Jin, G., Tang, M. and Cheng, G. (2011). The promotion of neurite sprouting and outgrowth of mouse hippocampal cells in culture by graphene substrates. Biomaterials, 32(35), 9374

7. Veliev, F., Briançon-Marjollet, A., Bouchiat, V., and Delacour, C. (2016). Impact of crystalline quality on neuronal affinity of pristine graphene. Biomaterials, 86, 33

8. Lee, C., Wei, X., Kysar, J. W., Hone, J. (2008). Measurement of the elastic properties and intrinsic strength of monolayer graphene. science, 321(5887), 385

9. S. Chen, L. Brown, M. Levendorf, W. Cai, S.-Y. Ju, J. Edgeworth, X. Li, C.W. Magnuson, A. Velamakanni, R.D. Piner, J. Kang, J. Park, R.S. Ruoff (2011). Oxidation resistance of graphene-coated Cu and Cu/Ni alloy, ACS Nano 5,1321

10. D. Prasai, J.C. Tuberquia, R.R. Harl, G.K. Jennings, B.R. Rogers, K.I. Bolotin (2012). Graphene: corrosion-inhibiting coating, ACS Nano 6, 1102

11. Geim, A.K., Novoselov, K.S (2007). The rise of graphene. Nat Mater. 6, 183

12. Singh, V., Joung, D., Zhai, L., Das, S., Khondaker, S.I., Seal, S. (2011). Graphene based materials: Past, present and future. Prog. Mater. Sci. 56, 1178

13. Girish, C. M., Sasidharan, A., Gowd, G. S., Nair, S., Koyakutty, M. (2013). Confocal Raman imaging study showing macrophage mediated biodegradation of graphene in vivo. Advanced healthcare materials, 2(11), 1489

14. Kotchey, G. P., Allen, B. L., Vedala, H., Yanamala, N., Kapralov, A. A., Tyurina, Y. Y., Klein-Seetharaman, J., Kagan, V.E., Star, A. (2011). The enzymatic oxidation of graphene oxide. ACS nano, 5(3), 2098

15. Kurapati, R., Russier, J., Squillaci, M. A., Treossi, E., Ménard-Moyon, C., Rio-Castillo, D., Vazquez, E., Samori, P., Palermo, V., Bianco, A. (2015). Dispersibility-Dependent Biodegradation of Graphene Oxide by Myeloperoxidase. Small, 11(32), 3985

16. Minev, I. R., Musienko, P., Hirsch, A., Barraud, Q., Wenger, N., Moraud, E. M., Gandar, J., Capogrosso, M., Milekovic, T., Asboth, L., Torres, R.F., Vachicouras, N., Liu, Q., Pavlova, N., Duis, S., Larmagnac, A., Vörös, J., Micera, S., Suo, Z., Courtine, G., Lacour, S.P. (2015). Electronic dura mater for long-term multimodal neural interfaces. Science, 347(6218), 159

17. Highley, C. B., Prestwich, G. D., Burdick, J. A. (2016). Recent advances in hyaluronic acid hydrogels for biomedical applications. Current opinion in biotechnology, 40, 35

18. Burdick, J. A., Prestwich, G. D. (2011). Hyaluronic acid hydrogels for biomedical applications. Advanced materials, 23(12).

19. Tarus, D., Hamard, L., Caraguel, F., Wion, D., Szarpak-Jankowska, A., van der Sanden, B., Auzély-Velty, R. (2016). Design of hyaluronic acid hydrogels to promote neurite outgrowth in three dimensions. ACS applied materials & interfaces, 8(38), 25051

20. Knopf-Marques, H., Pravda, M., Wolfova, L., Velebny, V., Schaaf, P., Vrana, N. E., Lavalle, P. (2016). Hyaluronic acid and its derivatives in coating and delivery systems: applications in tissue engineering, regenerative medicine and immunomodulation. Advanced healthcare materials, 5(22), 2841

21. Lee, J. Y., Khaing, Z. Z., Siegel, J. J., Schmidt, C. E. (2015). Surface modification of neural electrodes with a pyrrole-hyaluronic acid conjugate to attenuate reactive astrogliosis in vivo. RSC Advances, 5(49), 39228

22. Laszig, R., Ridder, G. J., Fradis, M. (2002). Intracochlear insertion of electrodes using hyaluronic acid in cochlear implant surgery. The Journal of Laryngology & Otology, 116(5), 371

23. Sridar, S., Churchward, M. A., Mushahwar, V. K., Todd, K. G., Elias, A. L. (2017). Peptide modification of polyimide-insulated microwires: Towards improved biocompatibility through reduced glial scarring. Acta Biomaterialia, 60, 154

24. Grand, L., Wittner, L., Herwik, S., Göthelid, E., Ruther, P., Oscarsson, S., Neves, H., Dombovari, B., Csercsa, R., Karmos, G., Ulbert, I. (2010). Short and long term biocompatibility of NeuroProbes silicon probes. Journal of neuroscience methods, 189(2), 216

25. Z. Han, A. Kimouche, D. Kalita, A. Allain, H. Arjmandi-Tash, A. Reserbat-Plantey, L. Marty, S. Pairis, V. Reita, N. Bendiab, J. Coraux, V. Bouchiat (2014). Homogeneous optical and electronic properties of graphene due to the suppression of multilayer patches during CVD on copper foils, Adv. Funct. Mater. 24, 964e970.

26. Kadi, S., Cui, D., Bayma, E., Boudou, T., Nicolas, C., Glinel, K., Picart, C., Auzély-Velty, R. (2009). Alkylamino hydrazide derivatives of hyaluronic acid: synthesis, characterization in semidilute aqueous solutions, and assembly into thin multilayer films. Biomacromolecules, 10(10), 2875

27. Schneider, C.A., Rasband, W.S., Eliceiri, K.W. (2012). NIH Image to ImageJ: 25 years of image analysis. Nat Methods 9, 671

28. DiGiovanna, J., Dominici, N., Friedli, L., Rigosa, J., Duis, S., Kreider, J., Beauparlant, J., van den Brand, R., Schieppati, M., Micera, S., and Courtine, G. (2016). Engagement of the Rat Hindlimb Motor Cortex across Natural Locomotor Behaviors. Journal of Neuroscience, 36(40), 10440

29. Veliev, F., Han, Z., Kalita, D., Briançon-Marjollet, A., Bouchiat, V., and Delacour, C. (2017). Recording spikes activity in cultured hippocampal neurons using flexible or transparent graphene transistors. Frontiers in Neuroscience, 11, 466

30. Lee, I. C., Wu, Y. C., Cheng, E. M., and Yang, W. T. (2015). Biomimetic niche for neural stem cell differentiation using poly-L-lysine/hyaluronic acid multilayer films. Journal of biomaterials applications, 29(10), 1418

31. Schneider, A., Francius, G., Obeid, R., Schwinté, P., Hemmerlé, J., Frisch, B., Schaaf, P., Voegel J.C., Senger, B., and Picart, C. (2006). Polyelectrolyte multilayers with a tunable Young's modulus: influence of film stiffness on cell adhesion. Langmuir, 22(3), 1193

32. Wenger, N., Moraud, E. M., Raspopovic, S., Bonizzato, M., DiGiovanna, J., Musienko, P., Morari, M., Micera, S., and Courtine, G. (2014). Closed-loop neuromodulation of spinal sensorimotor circuits controls refined locomotion after complete spinal cord injury. Science translational medicine, 6(255), 255ra133

33. Borton, D., Bonizzato, M., Beauparlant, J., DiGiovanna, J., Moraud, E. M., Wenger, N., Musienko, P., Minev, I.R., Lacour, S.P., Millan, J., Micera, S., and Courtine, G. (2014). Corticospinal neuroprostheses to restore locomotion after spinal cord injury. Neuroscience research, 78, 21

34. Blaschke, B. M., Tort-Colet, N., Guimerà-Brunet, A., Weinert, J., Rousseau, L., Heimann, A., Drieschner, S., Kempski, O., Villa, R., Sanchez-Vives, M.V., and Garrido, J. A. (2017). Mapping brain activity with flexible graphene micro-transistors. 2D Materials, 4(2), 025040

35. Bansil, R., Yannas, I. V., and Stanley, H. E. (1978). Raman spectroscopy: a structural probe of glycosaminoglycans. Biochimica et Biophysica Acta (BBA)-General Subjects, 541(4), 535

36. Barrett, T. W., and Peticolas, W. L. (1979). Laser Raman inelastic light scattering investigations of hyaluronic acid primary and secondary structure. Journal Of Raman Spectroscopy, 8(1), 35

37. Das, A., Chakraborty, B., and Sood, A. K. (2008). Raman spectroscopy of graphene on different substrates and influence of defects. Bulletin of Materials Science, 31(3), 579

38. Chang, H., Tang, L., Wang, Y., Jiang, J., and Li, J. (2010). Graphene fluorescence resonance energy transfer aptasensor for the thrombin detection. Analytical Chemistry, 82(6), 2341

39. Wang, Y., Yang, R., Shi, Z., Zhang, L., Shi, D., Wang, E., Zhang, G. (2011). Super-elastic graphene ripples for flexible strain sensors. ACS nano, 5(5), 3645

40. Xia, J., Chen, F., Li, J., and Tao, N. (2009). Measurement of the quantum capacitance of graphene. Nature nanotechnology, 4(8), 505

41. Ferreira, A., Viana-Gomes, J., Nilson, J., Mucciolo, E.R., Peres, N.M.R., Castro Neto, A.H., P. Phys., Rev., B, 2011, 83, 165402

42. Peres, N.M.R., Rev. Mod. Phys. 2010, 82, 2673

43. Vieira, N. C. S., Borme, J., Machado Jr, G., Cerqueira, F., Freitas, P. P., Zucolotto, V., Peres, NMR. and Alpuim, P. (2016). Graphene field-effect transistor array with integrated electrolytic gates scaled to 200 mm. Journal of Physics: Condensed Matter, 28(8), 085302

44. Kurisawa, M., Chung, J. E., Yang, Y. Y., Gao, S. J., and Uyama, H. (2005). Injectable biodegradable hydrogels composed of hyaluronic acid–tyramine conjugates for drug delivery and tissue engineering. Chemical communications, (34), 4312